

Dynamically emergent correlations in bosons via quantum resetting

Manas Kulkarni

International Centre for Theoretical Sciences, Tata Institute of Fundamental Research, Bangalore 560089, India
Email: manas.kulkarni@icts.res.in

Satya N. Majumdar

LPTMS, CNRS, Université Paris-Sud, Université Paris-Saclay, 91405 Orsay, France
Email: satya.majumdar@universite-paris-saclay.fr

Sanjib Sabhapandit

Raman Research Institute, Bangalore 560080, India
Email: sanjib@rri.res.in

Abstract. We study the nonequilibrium stationary state (NESS) induced by quantum resetting of a system of N noninteracting bosons in a harmonic trap. Our protocol consists of preparing initially the system in the ground state of a harmonic oscillator centered at $+a$, followed by a rapid quench where the center is shifted to $-a$ and the system is allowed to evolve unitarily up to a random Poissonian time τ distributed via $r e^{-r\tau}$. Then the trap center is reset to $+a$ again and the system is assumed to cool instantaneously to the initial ground state. The system is again allowed to evolve unitarily in the trap centered at $-a$ up to a random time, and the procedure is repeated. Under repeated resetting, the system reaches a NESS where the positions of bosons get *strongly correlated* due to simultaneous resetting induced by the trap. We fully characterize the steady state by analytically computing several physical observables such as the average density, extreme value statistics, order and gap statistics, and also the distribution of the number of particles in a region $[-L, L]$, known as the full counting statistics (FCS). In particular, we show that in the large N limit, the scaling function describing the FCS exhibits a striking feature: it is supported over a nontrivial finite interval, and moreover is discontinuous at an interior point of the support. Our results are supported by numerical simulations. This is a rare example of a strongly correlated quantum many-body NESS where various observables can be exactly computed.

Contents

| | | |
|----------|--|-----------|
| 1 | Introduction | 3 |
| 2 | Model and Quantum Resetting | 6 |
| 2.1 | Preparation of the initial state | 6 |
| 2.2 | Unitary evolution in the absence of resetting | 7 |
| 2.3 | Time evolution in the presence of quantum resetting | 8 |
| 3 | Observables | 11 |
| 3.1 | Average density profile | 12 |
| 3.2 | Correlation functions | 14 |
| 3.3 | Order and gap statistics | 14 |
| 3.3.1 | Distribution of the maximum (rightmost particle): | 15 |
| 3.3.2 | Distribution of the k -th maximum | 15 |
| 3.3.3 | Gap statistics: | 15 |
| 3.4 | Full Counting Statistics | 16 |
| 3.4.1 | Regime I: $\kappa_{\min} \leq \kappa < \kappa^*$: | 19 |
| 3.4.2 | Regime II: $\kappa^* \leq \kappa \leq \kappa_{\max}$: | 19 |
| 3.4.3 | Generalizing FCS to arbitrary domain $[L_1, L_2]$: | 22 |
| 4 | Numerical simulation procedure | 22 |
| 5 | Summary and Outlook | 23 |
| 6 | Acknowledgements | 24 |

1. Introduction

Quantum gases have been a subject of intense theoretical and experimental studies over several decades. In particular, a gas of interacting bosons, realized in cold atom systems, has been extensively studied [1–3]. Despite a plethora of progress, exact analytically tractable models for correlated bosonic gases are hardly available. For bosonic systems, two commonly studied models are the Lieb–Liniger model [4–6] and the Gross-Pitaevski equation [7–9]. Lieb–Liniger model describes a Bose gas with Dirac delta interaction in one spatial dimension. This quantum model is integrable, in the sense that its solution can be written in the form of a Bethe ansatz. Although several aspects of the Lieb–Liniger model have been extensively studied [10–13], especially given its integrability property, explicit solutions of various observables, such as the extreme value and the order statistics, the full counting statistics (FCS) have remained elusive. Furthermore, the inevitable presence of external confining traps (mostly harmonic) in experimental setups breaks the integrability, making calculations even more challenging. Another well-studied model that often describes the collective behaviour of a weakly interacting Bose gas is the Gross-Pitaevski equation. This is a continuum one-dimensional model that is integrable. Despite its integrability, it is a nonlinear partial differential equation, and therefore, exact solutions for observables remain challenging. Once again, in the presence of a confining trap, this integrable structure is broken making computations even more evasive [1]. Thus, there is a growing need to engineer and study correlated Bose gas which is also analytically tractable, in addition to being experimental feasible. It is hence natural to explore experimentally feasible correlated particle systems for which several observables can be computed analytically.

Recently, a new type of correlated gases has been found in classical systems where the correlations between particles are not inbuilt but are rather induced by the dynamics itself, e.g., by simultaneous resetting of independent Brownian particles [14]. Despite the presence of strong correlations in the stationary state, these models are solvable because of a special structure of the joint probability density function (JPDF) in the stationary state, namely, the conditionally independent and identically distributed (CIID) structure [14]

$$P_{\text{st}}(x_1, x_2, \dots, x_N) = \int_{-\infty}^{\infty} du h(u) \prod_{j=1}^N p(x_j|u). \quad (1)$$

The JPDF $P_{\text{st}}(x_1, x_2, \dots, x_N)$ in (1) is clearly not factorizable, thus rendering the gas correlated. However, inside the integral, for a fixed value of the parameter u , there is a factorizable structure. One can interpret this as follows. For a fixed u , the $\{x_i\}$ variables are independent, each drawn from a probability density function (PDF) $p(x|u)$ parametrized by u . But the parameter u itself is a random variable distributed via the PDF $h(u)$. Once integrated over u , the JPDF loses the factorizability. The advantage of the JPDF having a CIID structure is as follows. For an ideal gas without interaction (but with a certain parameter u fixed), several physical observables can be

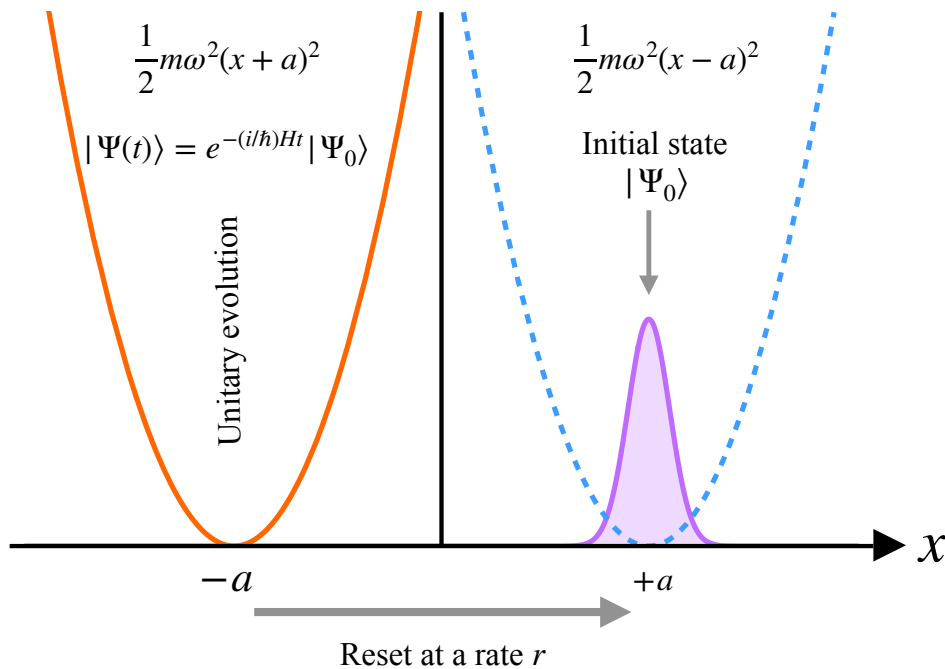


Figure 1. A schematic representation of the quantum resetting protocol. A system of N noninteracting bosons is prepared in the ground state of a quantum harmonic oscillator of frequency ω and centered at $x = +a$. The system evolves unitarily with a harmonic oscillator Hamiltonian H centered at $x = -a$, up to a random time drawn from an exponential distribution $r e^{-r\tau}$. After this random time, the trap center is moved instantaneously to $x = +a$, as shown by the arrow at the bottom, and the system is allowed to cool to the ground state – this is the resetting to the initial state. The cycle is repeated again. This quantum resetting drives the system into a nonequilibrium steady state where the bosons get strongly correlated.

easily computed analytically and one then needs to average over the parameter u drawn from its distribution $h(u)$ as in (1). In a series of recent works, this CIID structure (1) in the stationary state has been found in several classical models in one dimension [14–17].

Stochastic resetting [18–22] has emerged as a major area of research in statistical physics in recent times. While most of these studies focussed on resetting in classical systems, there have been few studies on quantum resetting [23–35]. In this paper, we study a quantum gas of noninteracting bosons in a trap subjected to stochastic resetting of the many-body quantum state to the initial state. We find that this quantum system reaches a nonequilibrium stationary state (NESS) that also has the above CIID structure (1), thus allowing exact calculation of several observables. This thus presents a much-needed new solvable strongly correlated quantum gas.

In our setup, the quantum resetting protocol is described as follows [see figure 1]. Initially, we prepare a system of N noninteracting bosons in the ground state of a quantum harmonic oscillator (harmonic trap), of frequency ω and centered at $x = +a$. Such a system of noninteracting bosons may be realized experimentally in optical traps where the interactions between the bosons can be effectively tuned to zero via Feshbach

resonance [36, 37]. We then instantaneously quench the trap center from $+a$ to $-a$ and let the system evolve unitarily up to a random Poissonian time τ distributed via $r e^{-r\tau}$. Following this, the trap center is instantaneously quenched back to $+a$ and the system is cooled to its initial ground state. This cooling can be achieved by coupling to a heat bath, and we do not make any measurements during this cooling period. This mimics instantaneous resetting as in the optical trap experiments in classical resetting [38, 39]. This procedure is repeated, and eventually, the system reaches a NESS. Thus our protocol has three main parameters (a, ω, r) . We show that even though there is no direct interaction between the bosons, the repeated resetting of the trap center dynamically induces an effective all-to-all correlation between the bosons that persist even at long times. This becomes manifest in the fact that the quantum JPDF of N bosons in the NESS is not factorizable. We considered this particular setup consisting of shifting the center of the oscillator from $a \rightarrow -a$ and resetting it back to $+a$ for two reasons. First, the initial state (centered around $x = +a$) is not an eigenstate of the Hamiltonian H . Secondly, the unitary evolution under H preserves the Gaussian form of the initial state at all times, thereby making it amenable to analytical computations.

The goal of this paper is to show that the NESS reached under this quantum resetting protocol has the CIID structure, i.e., the quantum JPDF can be expressed as in (1). This allows us to calculate several physical observables analytically in the large N limit. These observables include the average particle density profile, two-point correlation functions, extreme and order statistics, distribution of the spacing between two adjacent particles (i.e., gap statistics), the statistics of the total number of particles in a given interval, i.e., the full counting statistics (FCS). Some of these observables are global, while the others are local. These observables have been studied extensively in one-dimensional classical correlated gases, e.g., in the eigenvalue statistics of a Gaussian random matrix [40, 41] or its formulation as Dyson's log gas [42–46], Calogero model [46], Jellium model of one-dimensional one-component plasma [47–50]. More recently, such observables have also been studied in the Riesz gas [51–56]. Observables such as the average particle density and the statistics of the total number of particles in an interval can, in principle, be measured via absorption imaging techniques [57–60]. On the other hand, local observables such as the order statistics, and in particular, the statistics of the rightmost particle can be potentially accessed by quantum gas microscopy [61–64], where the resolution at the level of a single atom is feasible. Therefore, our proposed setup may be experimentally feasible, both in terms of designing the protocol as well as measuring the observables.

We briefly summarize our main findings:

- (i) We show that under the quantum resetting protocol mentioned above, the system reaches a steady state where the quantum JPDF $P_r(x_1, x_2, x_3 \dots, x_N)$ exhibits a CIID structure (25), as in (1). We identify the random variable u and its exact

PDF $h(u)$ [see equation (32)].

- (ii) We show that, in the steady state, the average density profile undergoes interesting shape transitions with respect to the resetting rate r and the trap frequency ω for a fixed a [see figure 3].
- (iii) The two-point correlation function in the steady state is given by

$$C_{i,j} = \langle x_i x_j \rangle - \langle x_i \rangle \langle x_j \rangle = \frac{4a^2 [5(r/\omega)^2 + 2]}{[(r/\omega)^2 + 1]^2 [(r/\omega)^2 + 4]} + \delta_{i,j} \frac{\hbar}{2m\omega}, \quad (2)$$

where m is the mass and \hbar is the Plank's constant. The function in (2) is positive, indicating an effective all-to-all attraction between bosons emerging due to simultaneous resetting.

- (iv) Strong correlations lead to extreme value and order statistics drastically different from that of independent and identically distributed (IID) and weakly correlated random variables [see figure 5].
- (v) The distribution of the number of bosons N_L within the domain $[-L, L]$, known as the full counting statistics (FCS), shows rather interesting behaviour [see figure 8]. For any finite L , there is a minimum fraction of $N_L/N > 0$ and a maximum fraction of $N_L/N < 1$ beyond which the FCS vanishes in the thermodynamic limit $N \rightarrow \infty$. In other words, it has non-trivial finite support. In addition, remarkably, the FCS displays a discontinuity and an integrable divergence at an intermediate point inside the support [see figure 8].

The paper is organized as follows. In section 2, we discuss the details of our model and the quantum resetting protocol. We obtain an interesting N -particle JPDF that turns out to be of CIID form. In section 3, we exploit the rich CIID structure to derive various observables. Perfect agreement is demonstrated between our analytical results and direct numerical simulations. We briefly describe the numerical simulation procedure used in the paper in section 4. In section 5, we summarize our results along with an outlook.

2. Model and Quantum Resetting

In this section, we will first describe the initial state preparation of N noninteracting bosons in a harmonic trap and then the unitary evolution of the system in the absence of resetting. Following this, we will describe the time evolution of this system in the presence of quantum resetting.

2.1. Preparation of the initial state

We prepare an initial state of N noninteracting bosons in the ground state of a quantum harmonic potential

$$V(x) = \frac{1}{2}m\omega^2(x - a)^2 \quad (3)$$

centered around $x = +a$, where m is the mass and ω is the trap frequency. The many-body ground state wavefunction is given by

$$\Psi_0(x_1, x_2, \dots, x_N) = \prod_{j=1}^N \psi_0(x_j) \quad (4)$$

where

$$\psi_0(x) = A_0 e^{-\frac{1}{2\sigma^2}(x-a)^2} \quad \text{with} \quad \sigma = \sqrt{\frac{\hbar}{m\omega}} \quad \text{and} \quad A_0 = \left(\frac{1}{\pi\sigma^2}\right)^{1/4}. \quad (5)$$

The subscript ‘0’ in (4) and (5) stands for the ‘ground state’. The ground state in (4) is our initial state.

2.2. Unitary evolution in the absence of resetting

Starting from the initial state (4), the system is evolved unitarily by the following quantum harmonic oscillator Hamiltonian centered around $x = -a$

$$H = \sum_{j=1}^N \left[\frac{p_j^2}{2m} + \frac{1}{2} m \omega^2 (x_j + a)^2 \right]. \quad (6)$$

The subsequent time evolution of (4) according to (6) takes the form

$$\Psi(x_1, x_2, \dots, x_N, t) = \prod_{j=1}^N \psi(x_j, t), \quad (7)$$

where

$$\psi(x, t) = \int_{-\infty}^{\infty} K(x + a, y + a, t) \psi_0(y) dy. \quad (8)$$

The Mehler Kernel $K(x, y, t) \equiv \langle x | e^{-iHt} | y \rangle$ in (8) is given by [65]

$$K(x, y, t) = \frac{1}{\sqrt{2\pi i \sigma^2 \sin(\omega t)}} \exp \left(\frac{i}{2\sigma^2 \sin(\omega t)} [(x^2 + y^2) \cos(\omega t) - 2xy] \right). \quad (9)$$

Since the Kernel and initial state are both of Gaussian form, the single-particle wavefunction $\psi(x, t)$ in (8) remains Gaussian at all times, i.e.,

$$\psi(x, t) = A(t) e^{-\frac{1}{2\sigma(t)^2} (x - \mu(t))^2}. \quad (10)$$

Using (9) in (8), we get

$$\mu(t) = 2ae^{-i\omega t} - a, \quad \sigma(t) = \sigma, \quad A(t) = A_0 e^{-i\omega t/2} \exp \left[-\frac{a^2}{\sigma^2} (1 - e^{-2i\omega t}) \right]. \quad (11)$$

As pointed out earlier, this preservation of the Gaussian structure during the unitary dynamics is our primary motivation for choosing this setup. The N -particle JPDF is given by

$$P(x_1, x_2, \dots, x_N, t) = |\Psi(x_1, x_2, \dots, x_N, t)|^2 = \prod_{j=1}^N |\psi(x_j, t)|^2 = \prod_{j=1}^N p(x_j, t), \quad (12)$$

where the single-particle PDF from (10) and (11) turns out to be

$$p(x, t) = |\psi(x, t)|^2 = \frac{1}{\sqrt{\pi\sigma^2}} e^{-\frac{1}{\sigma^2}(x - \mu_R(t))^2}, \quad (13)$$

with $\mu_R(t)$ representing the real part of $\mu(t)$,

$$\mu_R(t) \equiv \text{Re}[\mu(t)] = a(2 \cos(\omega t) - 1). \quad (14)$$

Interestingly, the width $\sigma(t) = \sigma$ of the single-particle PDF is time independent whereas the location $\mu_R(t)$ where the Gaussian is centered, oscillates between $x = -3a$ and $x = +a$ with a time period $T = 2\pi/\omega$. Finally, the N -particle quantum JPDF takes the explicit factorized form

$$P(x_1, x_2, \dots, x_N, t) = \prod_{j=1}^N \frac{1}{\sqrt{\pi\sigma^2}} e^{-\frac{1}{\sigma^2}(x_j - \mu_R(t))^2}, \quad (15)$$

indicating the absence of any correlations among the bosons.

2.3. Time evolution in the presence of quantum resetting

We now switch on the resetting with rate r . To see how the system evolves under the combined unitary ‘quantum’ dynamics and the ‘classical’ stochastic resetting dynamics, we start by recalling how the density matrix of a pure state evolves under resetting [23]. Consider a system initially in a pure state $|\Psi_0\rangle$. Under the unitary evolution with a time-independent Hamiltonian H , the state evolves as $|\Psi(t)\rangle = e^{-(i/\hbar)Ht}|\Psi_0\rangle$. Consequently, the density matrix $\varrho(t) = |\Psi(t)\rangle\langle\Psi(t)|$ evolves as

$$\varrho(t) = e^{-(i/\hbar)Ht} \varrho(0) e^{(i/\hbar)Ht} \quad \text{where } \varrho(0) = |\Psi_0\rangle\langle\Psi_0|. \quad (16)$$

The quantum resetting is a mixture of classical stochastic and quantum unitary evolution defined as follows [23]. In a small time dt , the state of the system evolves as

$$|\Psi(t + dt)\rangle = \begin{cases} |\Psi_0\rangle & \text{with prob. } r dt, \\ [1 - (i/\hbar)Hdt] |\Psi(t)\rangle & \text{with prob. } 1 - r dt, \end{cases} \quad (17)$$

where r represents the resetting rate. For $r = 0$, one recovers the unitary evolution. Under this quantum resetting dynamics, one can show that the density matrix $\varrho_r(t)$ evolves as [23]

$$\varrho_r(t) = e^{-rt} \varrho(t) + r \int_0^t d\tau e^{-r\tau} \varrho(\tau), \quad (18)$$

where $\varrho(t)$ is defined in (16) and the subscript ‘ r ’ in $\varrho_r(t)$ stands for ‘resetting’. This result is easy to understand from the renewal nature of the underlying stochastic process. The first term corresponds to the case when there is no resetting event in the interval $[0, t]$ and the system evolves unitarily up to t . The second term corresponds to events

where there are one or more resettings within $[0, t]$. In this latter case, it is enough to consider the epoch $t - \tau$ at which the last resetting event occurred before t . Then, during the interval $[t - \tau, t]$ the system evolves unitarily, explaining the presence of $\varrho(\tau)$ inside the integral of the second term in (18). Finally, the probability that there is no resetting event in the interval $[t - \tau, t]$, preceded by a resetting event within an interval $d\tau$ at the beginning of this interval is simply $r d\tau e^{-r\tau}$. Finally, integrating over τ from 0 to t , one gets the second term in (18).

The quantum JPDF of N particles with density matrix $\varrho_r(t)$ is given by the matrix element

$$P_r(x_1, x_2, \dots, x_N, t) = \langle x_1, x_2, \dots, x_N | \varrho_r(t) | x_1, x_2, \dots, x_N \rangle. \quad (19)$$

Computing this matrix element from (18), one gets

$$P_r(x_1, x_2, \dots, x_N, t) = e^{-rt} P(x_1, x_2, \dots, x_N, t) + r \int_0^t d\tau e^{-r\tau} P(x_1, x_2, \dots, x_N, \tau), \quad (20)$$

where $P(x_1, x_2, \dots, x_N, t)$ is given by

$$P(x_1, x_2, \dots, x_N, t) = |\Psi(x_1, x_2, \dots, x_N, t)|^2 = \langle x_1, x_2, \dots, x_N | \varrho(t) | x_1, x_2, \dots, x_N \rangle. \quad (21)$$

In our case, the quantum JPDF in the absence of resetting $P(x_1, x_2, \dots, x_N, t)$, is given by (15). As $t \rightarrow \infty$, the first term in (20) drops out and one arrives at a nonequilibrium steady state given by

$$P_r(x_1, x_2, \dots, x_N) = r \int_0^\infty d\tau e^{-r\tau} P(x_1, x_2, \dots, x_N, \tau). \quad (22)$$

Using (15) in (22), we explicitly get

$$P_r(x_1, x_2, \dots, x_N) = r \int_0^\infty d\tau e^{-r\tau} \prod_{j=1}^N \frac{1}{\sqrt{\pi\sigma^2}} e^{-\frac{1}{2\sigma^2} (x_j - \mu_R(\tau))^2}. \quad (23)$$

While (23) represents the steady state of the system undergoing resetting at a constant rate r , equation (23) can also be interpreted as follows:

- (i) We prepare the system in the ground state given by (4).
- (ii) We evolve it by the quantum Hamiltonian given in (6) for a random time τ drawn from an exponential distribution $r e^{-r\tau}$.
- (iii) At the end of this time we make a measurement for the positions of particles.
- (iv) The process (i, ii, iii) above is repeated to reconstruct a JPDF of the position of the particles.

This interpretation can be well suited for an experimental implementation as well as direct numerical simulations. It is evident from (23) that the JPDF in the presence of resetting does not have a trivial product form as was the case in (15), indicating strong correlations between the positions of the particles. As mentioned earlier, such

dynamically emerging strong correlation between noninteracting particles with a CIID structure was recently investigated in several classical systems [14–17]. However, such emergent dynamical correlations in quantum gases have been elusive so far.

As mentioned earlier, the observables of our interest include the average particle density profile, two-point correlation functions, extreme and order statistics, gap statistics, and FCS. In order to compute them, it is useful to make a change of variable from τ to a new variable u via the transformation

$$u = \mu_R(\tau) = a(2 \cos(\omega\tau) - 1) \quad \text{where } u \in [-3a, a]. \quad (24)$$

As a result, (23) becomes

$$P_r(x_1, x_2, \dots, x_N) = \int_{-3a}^a du h(u) \prod_{j=1}^N \frac{1}{\sqrt{\pi\sigma^2}} e^{-\frac{1}{\sigma^2}(x_j - u)^2}. \quad (25)$$

Under the change of variable from τ to u , the PDF $h(u)$ in (25) is given by

$$h(u) = \frac{r e^{-r\tau}}{|du/d\tau|} = \sum_{n=1}^{\infty} \frac{r e^{-r\tau_n}}{2a\omega |\sin(\omega\tau_n)|}, \quad (26)$$

where τ_n represents the n -th root of (24) for a given u . The root τ_1 in (26) denotes the principle value of inverse cosine

$$\tau_1 = \frac{1}{\omega} \cos^{-1} \left[\frac{1}{2} \left(1 + \frac{u}{a} \right) \right] \quad \text{where } \omega\tau_1 \in [0, \pi]. \quad (27)$$

The other roots of (24), i.e., $\omega\tau_n \notin [0, \pi]$ are related to the principle root τ_1 by

$$\tau_{2s} = \frac{2s\pi}{\omega} - \tau_1 \quad \text{where } \omega\tau_{2s} \in [(2s-1)\pi, 2s\pi] \quad \text{with } s = 1, 2, \dots, \infty \quad (28)$$

$$\tau_{2s+1} = \frac{2s\pi}{\omega} + \tau_1 \quad \text{where } \omega\tau_{2s+1} \in [2s\pi, (2s+1)\pi] \quad \text{with } s = 1, 2, \dots, \infty \quad (29)$$

We note that $|\sin(\omega\tau_n)|$ that appears in (26) is independent of index n and is given by $|\sin(\omega\tau_n)| = \sqrt{1 - \frac{1}{4}(1 + u/a)^2}$. Therefore, (26) becomes

$$h(u) = \frac{r/\omega}{\sqrt{4a^2 - (a+u)^2}} \sum_{n=1}^{\infty} e^{-r\tau_n}. \quad (30)$$

The summation in (30) can be split into odd and even values of n . Subsequently using (28) and (29), the summation can be performed explicitly and we get

$$h(u) = \frac{(r/\omega) \cosh \left[(r/\omega)(\pi - \omega\tau_1) \right]}{\sinh[\pi r/\omega] \sqrt{4a^2 - (a+u)^2}}. \quad (31)$$

where τ_1 is given in (27). This further simplifies the PDF in (31) to

$$h(u) = \frac{\tilde{r}}{\sinh(\pi\tilde{r})} \frac{1}{\sqrt{4a^2 - (a+u)^2}} \cosh \left[\tilde{r} \left(\pi - \cos^{-1} \left(\frac{1}{2}(1 + u/a) \right) \right) \right] \quad \text{with } \tilde{r} = \frac{r}{\omega}, \quad (32)$$

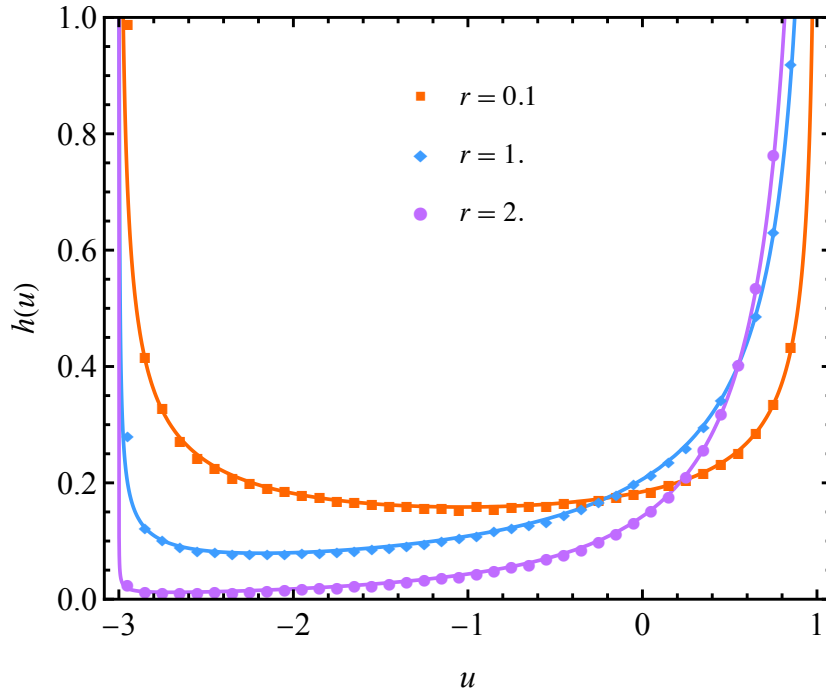


Figure 2. The solid lines plot the PDF $h(u)$ given in (32) as a function of u for three different values of $r = 0.1, 1.0, 2.0$, keeping $\omega = 1, a = 1$. The points are obtained from numerical simulations with 64×10^4 realizations.

where $u \in [-3a, a]$. In figure 2, we show the PDF $h(u)$ in (32) for three representative values of the resetting rate. Near the edges of the support $u \in [-3a, a]$, the function takes the form,

$$h(u) = \frac{\tilde{r}}{2\sqrt{a} \sinh(\pi\tilde{r})} \times \begin{cases} \frac{1}{\sqrt{3a+u}} + O(\sqrt{3a+u}) & \text{as } u \rightarrow -3a, \\ \frac{\cosh(\pi\tilde{r})}{\sqrt{a-u}} + O(\sqrt{a-u}) & \text{as } u \rightarrow a. \end{cases} \quad (33)$$

Here, we remark that interestingly the JPDF structure in (25) was recently obtained for a classical gas of non-interacting particles in a harmonic potential whose center is driven by an independent stochastic process [17]. It is however, not at all evident whether $h(u)$ derived in this work [see equation (32)] can be obtained from a noninteracting classical gas studied in Ref. [17]. Nevertheless, the similarity in the mathematical structure in the JPDF enables us to adapt many of the approaches in Ref. [17] to compute some of the observables mentioned above. Starting with (25) and (32), we evaluate several observables in Sec. 3.

3. Observables

In this section, we discuss various observables for the correlated bosonic gas.

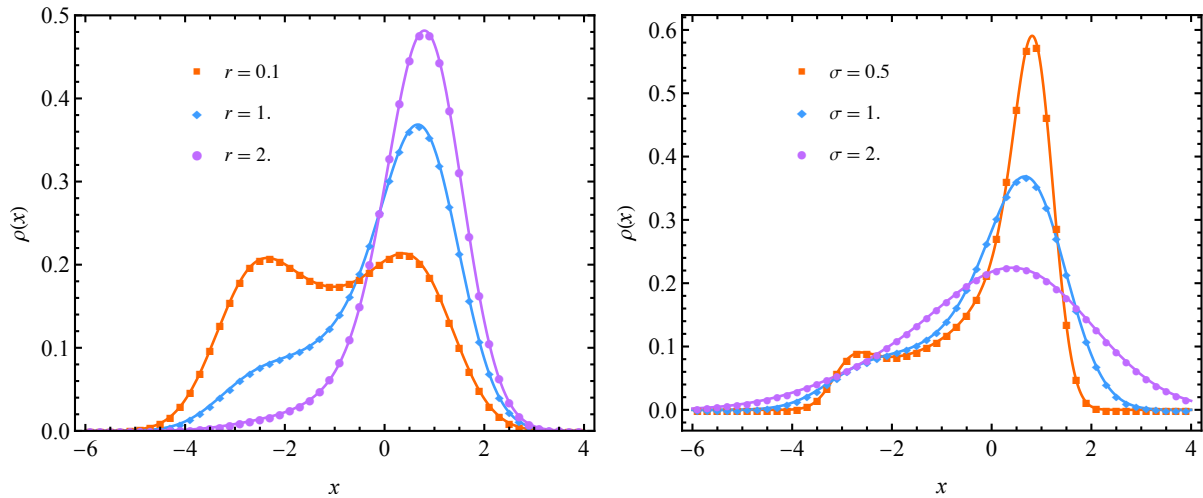


Figure 3. (Left) The spatial density profile $\rho(x)$ vs. x in the steady state with $\sigma = 1$ for $r = 0.1, 1.0, 2.0$. (Right) The spatial density profile with $r = 1$ for $\sigma = 0.1, 1.0, 2.0$. The solid lines plot equation (35) and the points are obtained from numerical simulations with 64×10^4 realizations and $N = 10^4$.

3.1. Average density profile

A natural observable that enables one to characterize a cloud of gas is the average density profile,

$$\rho(x) = \left\langle \frac{1}{N} \sum_{i=1}^N \delta(x - x_i) \right\rangle. \quad (34)$$

where the average $\langle \cdots \rangle$ is with respect to the JPDP given in (25). Evaluating (34), we get

$$\rho(x) = \frac{1}{\sqrt{\pi\sigma^2}} \int_{-3a}^a du h(u) \exp\left(-\frac{(x-u)^2}{\sigma^2}\right), \quad (35)$$

where $h(u)$ is given in (32). Furthermore, the density in (35) can be expressed as a scaling function of x/a together with two independent dimensionless parameters r/ω and σ/a . This is essentially equivalent to setting $\omega = 1$ and $a = 1$. In figure 3, we plot the density in (35) for various values of r for a fixed σ and various values of σ for a fixed r . We find interesting shape transitions with respect to both r and σ . We find that for a fixed σ , there is a critical resetting rate r^* across which the density profile exhibits a bimodal to a unimodal transition. Likewise, for a fixed r , there is a critical σ^* where the density profile undergoes a similar transition.

To understand this shape transition, it is useful to look at the two extreme limits $r \rightarrow 0$ and $r \rightarrow \infty$. In the $r \rightarrow 0$ limit, the evolution is essentially given by (15) and we observe the system at random times with uniform distribution $\omega/2\pi$ in a given period $[0, 2\pi/\omega]$. It is then easy to show that the distribution of the location $u = \mu_R(t)$ [see equation (24)] of the Gaussian is given by

$$h(u) = \frac{1}{\pi\sqrt{4a^2 - (a+u)^2}} \quad \text{for } r \rightarrow 0. \quad (36)$$

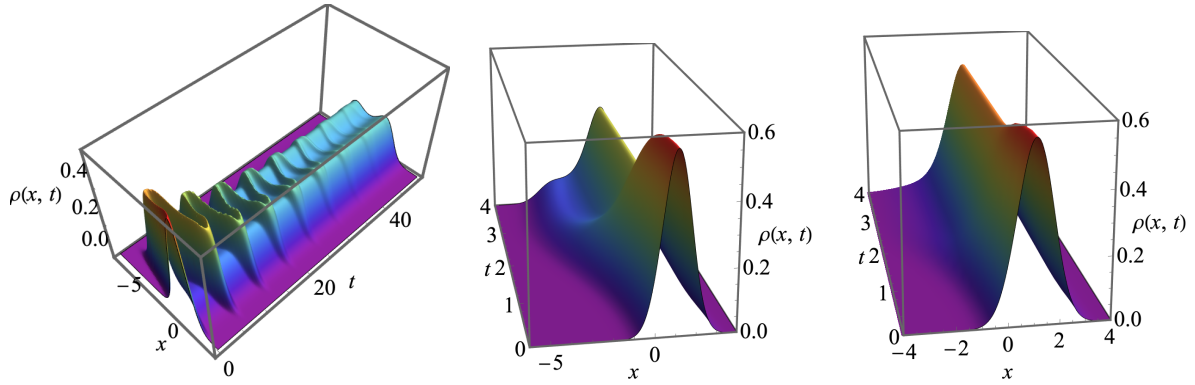


Figure 4. Space-time plots of the average density profile $\rho(x, t)$ vs. x with time t as the other axis, for $r = 0.1$ (left), $r = 1.0$ (middle), and $r = 2.0$ (right). The figure shows that the density profile in the presence of resetting given by (38) oscillates in time, and the oscillations eventually diminish as time progresses. Eventually, the profile reaches a corresponding steady state shown in figure 3. We set $a = 1$ and $\sigma = 1$. The orientations of the figures are chosen to make the features best visible.

In fact, (36) can be obtained by taking the $r \rightarrow 0$ limit in (32). Subsequently, the density is given by

$$\rho(x) = \frac{1}{\sqrt{\pi\sigma^2}} \int_{-3a}^a du \frac{1}{\pi\sqrt{4a^2 - (a+u)^2}} \exp\left(-\frac{(x-u)^2}{\sigma^2}\right), \quad (37)$$

which is a bimodal distribution for $\sigma/a < 1.591 \dots$ and unimodal otherwise. On the other hand, in the $r \rightarrow \infty$, we observe the system mostly in the initial state, which is centered around $x = a$, giving a unimodal structure to the distribution. Indeed, in the $r \rightarrow \infty$ limit, $h(u)$ in (32) approaches a Dirac delta function $\delta(u - a)$ resulting in $\rho(x) = 1/(\sigma\sqrt{\pi}) e^{-(x-a)^2/\sigma^2}$ for any σ . Therefore, as we interpolate from small to large r , the density profile undergoes a bimodal to a unimodal shape transition.

Approach to the steady state: So far, we have discussed the steady state properties of the system. However, our approach can be easily adapted to also study how the system relaxes to the stationary state at long times. For instance, the average density profile at any time t is given by

$$\rho(x, t) = e^{-rt} p(x, t) + r \int_0^t d\tau e^{-r\tau} p(x, \tau), \quad (38)$$

where $p(x, t)$ is the single-particle PDF in the absence of resetting given in (13) with (14). Unfortunately, the integral in (38) can not be carried out explicitly for finite t . However, one can easily plot $\rho(x, t)$ as a function of x , for fixed t , to see how the average density profile evolves with time and approaches the stationary profile as $t \rightarrow \infty$. This is shown in figure 4 for three values of the resetting rate r .

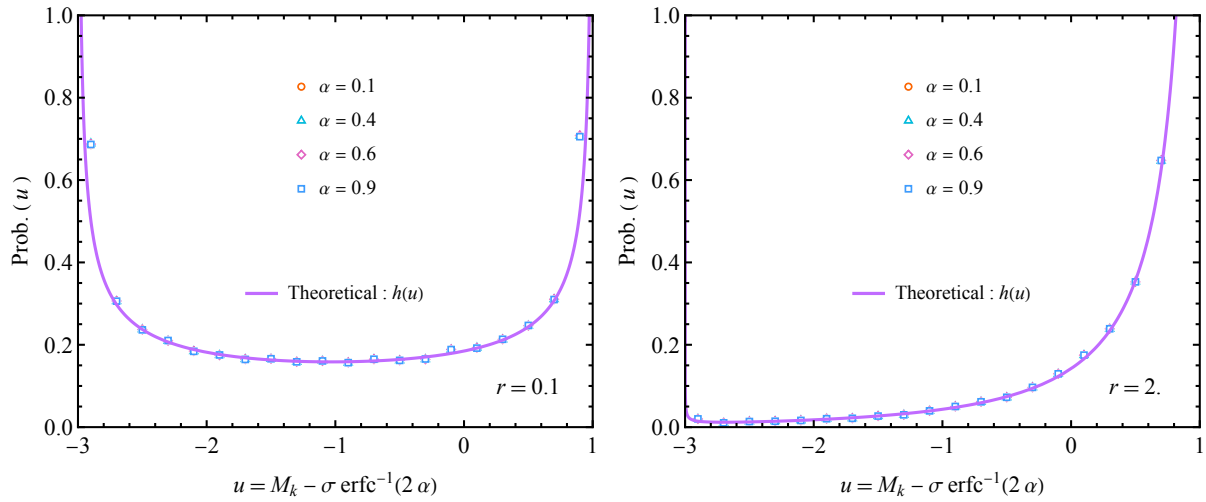


Figure 5. Order statistics, $\text{Prob.}[M_k - \sigma \text{erfc}^{-1}(2\alpha) = u]$ vs. u , for $r = 0.1$ (left) and $r = 2.0$ (right) for different values of $\alpha = k/N$ ranging from the right edge to the left edge via the bulk. The solid (theoretical) lines plot equation (45) where $h(u)$ is given by (32), and the points are obtained from numerical simulations with 7×10^5 realizations and $N = 10^6$. We set $\omega = 1$, $\sigma = 1$ and $a = 1$.

3.2. Correlation functions

In this subsection, we will discuss connected two-point correlation functions between the positions of the particles. It is defined in the stationary state as

$$C_{i,j} = \langle x_i x_j \rangle - \langle x_i \rangle \langle x_j \rangle, \quad (39)$$

where $\langle \dots \rangle$ is over the stationary measure (25). Following Ref. [17], we get

$$C_{i,j} = \text{Var}(u) + \delta_{i,j} \frac{\sigma^2}{2}, \quad (40)$$

where $\text{Var}(u)$ is the variance of u with respect to the stationary PDF $h(u)$, i.e.,

$$\text{Var}(u) = \langle u^2 \rangle - \langle u \rangle^2 = \int_{-\infty}^{\infty} u^2 h(u) du - \left[\int_{-\infty}^{\infty} u h(u) du \right]^2. \quad (41)$$

Using $h(u)$ from (32), we get

$$\text{Var}(u) = \frac{4a^2 (\tilde{r}^2 + 2)}{(\tilde{r}^2 + 1)^2 (\tilde{r}^2 + 4)} \quad \text{with} \quad \tilde{r} = \frac{r}{\omega}. \quad (42)$$

Interestingly $\text{Var}(u)$ in (42) is non-monotonic in \tilde{r} . It initially increases quadratically from $2a^2$, reaches a maximum at $\tilde{r} = 0.2734 \dots$, and then decreases monotonically with increasing \tilde{r} , eventually as \tilde{r}^{-4} for large \tilde{r} .

3.3. Order and gap statistics

While the average density profile discussed in section 3.1 gives the overall spatial structure of the correlated gas, the statistics of individual bosons remains elusive. In fact,

one expects the statistics of the particles in the bulk and the edges to be very different. To unravel these features, we investigate the order statistics, which is the statistics of the ordered position M_k of the k -th particle from the right. In other words, particle $M_1 = \max\{x_1, x_2, \dots, x_N\}$ denotes the position of the rightmost particle. Subsequently, the PDF of the M_k is given by

$$\text{Prob.}(M_k = w) = \int_{-3a}^a du h(u) \text{Prob.}(M_k(u) = w), \quad (43)$$

where $M_k(u)$ is the position of the k -th maxima for a set of N IID random variables drawn from a Gaussian distribution with mean u and variance $\sigma^2/2$. In addition to the order statistics, we present results for the statistics of the gap between k -th and $(k+1)$ -th particle.

3.3.1. Distribution of the maximum (rightmost particle): It is well known from the theory of extreme value statistics [14, 17, 66–69] that the distribution of the maximum of a set of Gaussian IID random variables, around its typical value $u + \sigma \sqrt{\ln N}$, is given by the Gumbel distribution whose width goes to zero as $1/\sqrt{\ln N}$. Therefore in the large- N limit, $\text{Prob.}(M_1(u) = w) \simeq \delta(w - u - \sigma^2 \sqrt{\ln N})$. As a consequence, from (43) with $k = 1$, we get

$$\text{Prob.}(M_1 = w) \simeq h\left(w - \sigma \sqrt{\ln N}\right), \quad (44)$$

where $h(u)$ is given in Equation (32).

3.3.2. Distribution of the k -th maximum Again from the theory of order statistics, the typical value of the k -th maximum of a set of IID Gaussian random variables is given by [14, 17, 66–68] $w^*(u) = u + \sigma \text{erfc}^{-1}(2\alpha)$, where $\alpha = k/N$ and erfc^{-1} is the inverse complementary error function, i.e., $\text{erfc}[\text{erfc}^{-1}(z)] = z$. Furthermore, the fluctuation around the typical value $w^*(u)$ goes to zero as $N \rightarrow \infty$. As a consequence, for large N , we have $\text{Prob.}(M_k(u) = w) \simeq \delta(w - w^*(u))$. Finally from (43), we get

$$\text{Prob.}(M_k = w) \simeq h\left(w - \sigma \text{erfc}^{-1}(2\alpha)\right). \quad (45)$$

In figure 5, we compare our analytical predictions of the order statistics given by (45) with numerical simulations for various values of α and find excellent agreement.

3.3.3. Gap statistics: We now discuss the statistics of the gap d_k between the k -th and $(k+1)$ -th particle. Let $d_k(u) = M_k(u) - M_{k+1}(u)$ represents the gap between the position of the k -th particle for a given u . Therefore, averaging over u , we get

$$\text{Prob.}(d_k = g) = \int_{-3a}^a du h(u) \text{Prob.}(M_k(u) - M_{k+1}(u) = g). \quad (46)$$

As described in Ref. [17], the statistics of the gap is fully independent of the PDF $h(u)$ given in (32). This is because the gap between particle positions does not depend on

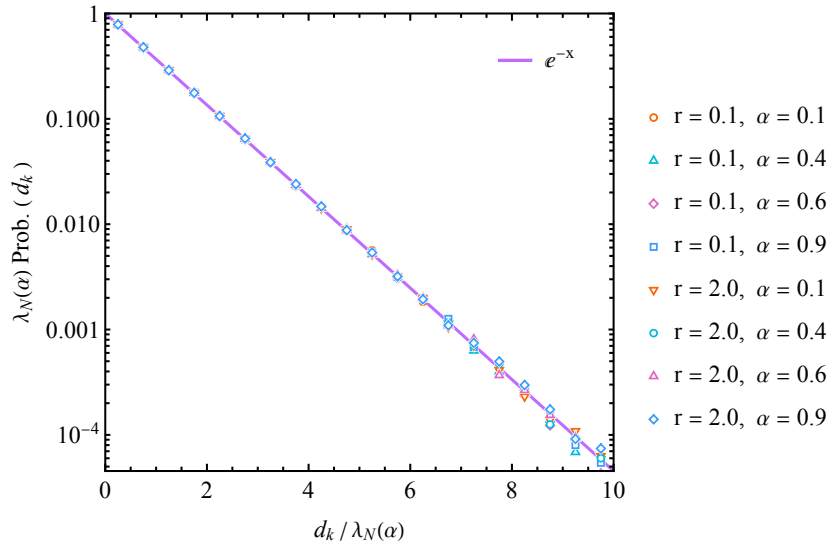


Figure 6. Scaling data collapse for the distribution $\text{Prob.}(d_k)$ of the k -th gap d_k as in (47) for different values of $\alpha = k/N$, σ , and r . The characteristic gap size $\lambda_N(\alpha)$ is given in (48). The points are obtained from numerical simulation with 7×10^5 realizations and $N = 10^6$. We set $\omega = 1$ and $a = 1$. The solid line plots the exponential function e^{-x} .

the shift parameter u which is common to all the x_i 's in (25). As a result, we get the same distribution as given in Ref. [17] which reads

$$\text{Prob.}(d_k = g) \simeq \frac{1}{\lambda_N(\alpha)} \exp\left(-\frac{g}{\lambda_N(\alpha)}\right), \quad (47)$$

where the characteristic gap size $\lambda_N(\alpha)$ is given by

$$\lambda_N(\alpha) = \left[\frac{N}{\sigma\sqrt{\pi}} \exp(-[\text{erfc}^{-1}(2\alpha)]^2) \right]^{-1}. \quad (48)$$

In figure 6, we compare the theoretical prediction given in (47) with numerical simulations and find excellent agreement for various values σ . Furthermore, we demonstrate that it is indeed independent of resetting rate r .

3.4. Full Counting Statistics

This section is devoted to the study of the full counting statistics (FCS) that describes the distribution of the number of particles N_L in a given region $[-L, L]$. Evidently, N_L is a random variable, and it will be interesting to study the probability distribution $P(N_L, N)$, for the correlated gas of N bosons described by the JPFD in (25). We show below that $P(N_L, N)$ exhibits very interesting behaviours. For large N and large N_L , with the ratio $N_L/N = \kappa$ fixed ($0 \leq \kappa \leq 1$), the FCS $P(N_L, N)$ has a scaling form

$$P(N_L, N) \simeq \frac{1}{N} H\left(\frac{N_L}{N}\right). \quad (49)$$

We find two surprising features of the FCS in (49):

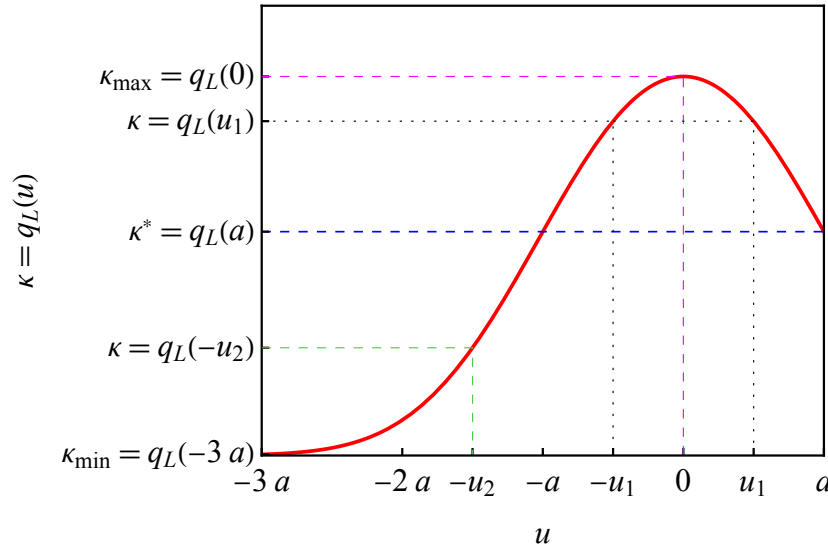


Figure 7. Plot of $\kappa = q_L(u)$ as a function of u , where $q_L(u)$ is given in (51). As the range of u in the integral given in (54) lies in $[-3a, a]$, the lower support of κ is given by $\kappa_{\min} = q_L(-3a)$ and is strictly positive. Similarly, the upper support of κ is given by $\kappa_{\max} = q_L(0)$ and is strictly less than unity for any $L < \infty$. It is important to note that for $\kappa_{\min} \leq \kappa < \kappa^* = q_L(-a)$, there is a unique u for a given κ (represented by green dashed line). On the contrary, for $\kappa^* \leq \kappa \leq \kappa_{\max}$, two values of u contribute to the integral in (54) for a given κ (represented by black dotted line).

- We show that the scaling function $H(\kappa)$ is supported over a finite interval $\kappa \in [\kappa_{\min}, \kappa_{\max}]$ that is different from $[0, 1]$, i.e., $\kappa_{\min} > 0$ and $\kappa_{\max} < 1$. Thus the fraction of particles that get accommodated in the region $[-L, L]$ cannot be less than κ_{\min} and also cannot be bigger than κ_{\max} . This is rooted in the fact that strong correlations are present in the gas. While for finite- N , the full range of $\kappa \in [0, 1]$ is allowed, the support $\kappa \in [\kappa_{\min}, \kappa_{\max}]$ becomes smaller only in the thermodynamic limit $N \rightarrow \infty$. A similar fact was noticed earlier in the FCS of classical systems [16, 17].
- A second dramatic feature of the FCS in our model is that there is an intermediate value $\kappa_{\min} < \kappa^* < \kappa_{\max}$ such that the scaling function $H(\kappa)$ displays different behaviours in the two regimes: (I) $\kappa_{\min} \leq \kappa < \kappa^*$ and (II) $\kappa^* \leq \kappa \leq \kappa_{\max}$. Moreover, the scaling function exhibits a discontinuity at $\kappa = \kappa^*$ [see figure 8]. The scaling function $H(\kappa)$ approaches a constant as κ approaches κ^* from below and has an integrable divergence as κ approaches κ^* from above. Below, we will discuss the two regimes separately.

Using the CIID structure of the JPDF in (25) and (32), one can express the FCS as

$$P(N_L, N) = \int_{-3a}^a du h(u) P(N_L, N|u), \quad (50)$$

where $P(N_L, N|u)$ is the FCS for a set of N IID random variables drawn from a Gaussian distribution with mean u and variance $\sigma^2/2$. For this set of IID Gaussian random

variables, the probability of finding each particle within the interval $[-L, L]$ is evidently,

$$q_L(u) = \int_{-L}^L \frac{1}{\sqrt{\pi\sigma^2}} e^{-\frac{1}{2\sigma^2}(x_j-u)^2} dx = \frac{1}{2} \left(\operatorname{erf} \left[\frac{L-u}{\sigma} \right] + \operatorname{erf} \left[\frac{L+u}{\sigma} \right] \right), \quad (51)$$

where $\operatorname{erf}(x)$ is the error function. Therefore, $P(N_L, N|u)$ is simply given by the binomial distribution,

$$P(N_L, N|u) = \binom{N}{N_L} [q_L(u)]^{N_L} [1 - q_L(u)]^{N-N_L}. \quad (52)$$

Before proceeding further, let us recall $\kappa = N_L/N$. It is straightforward to show from the Binomial distribution in (52) that the distribution of κ converges to a Gaussian distribution centered around $q_L(u)$ with a width proportional to $1/\sqrt{N}$. Hence in the large- N limit, equation (52) becomes

$$P(N_L = \kappa N, N|u) \rightarrow \frac{1}{N} \delta(\kappa - q_L(u)). \quad (53)$$

Consequently,

$$P(N_L, N) \simeq \frac{1}{N} H\left(\frac{N_L}{N}\right) \quad \text{with} \quad H(\kappa) = \int_{-3a}^a du h(u) \delta[\kappa - q_L(u)], \quad (54)$$

where $q_L(u)$ and $h(u)$ are given in (51) and (32) respectively. It is evident from (51) that $q_L(u) \rightarrow 1$ as $L \rightarrow \infty$. As a result from (54), we get $H(\kappa) \rightarrow \delta(\kappa - 1)$. This is consistent with the fact that for an infinite domain the probability of finding $N_L = N$ particles is obviously unity.

Below, we will see that all the interesting features of the scaling function $H(\kappa)$, mentioned in the beginning of this section, emerge from performing the integral in (54) for any finite L . In order to carry out the integral over delta function in (54), it is useful to plot $q_L(u) = \kappa$ in (51) as a function of u . This is shown in figure 7 where the allowed range of u is $[-3a, a]$. When $u = -3a$, i.e., at the lowest allowed point, the corresponding value of κ is given by

$$\kappa_{\min} = q_L(-3a). \quad (55)$$

Similarly, the maximum allowed value of κ for $u \in [-3a, a]$ occurs at the maximum of the function $q_L(u)$, i.e., at $u = 0$, and is given by

$$\kappa_{\max} = q_L(0). \quad (56)$$

We notice from figure 7 that the function $q_L(u)$ is non-monotonic in the range $u \in [-3a, a]$. As a result, the inverse function $u = q_L^{-1}(\kappa)$ has a single root for $\kappa_{\min} \leq \kappa < \kappa^*$ (regime I), while it has two roots for $\kappa^* \leq \kappa \leq \kappa_{\max}$ (regime II), where κ^* is given by

$$\kappa^* = q_L(-a) = q_L(a). \quad (57)$$

Therefore, we analyse $H(\kappa)$ in (54) separately in the two regimes I and II.

3.4.1. Regime I: $\kappa_{\min} \leq \kappa < \kappa^$:* Given that there is a unique value of $u \in [-3a, -a)$ for a given κ in this regime, we get

$$H(\kappa) = \int_{-3a}^{-a} du h(u) \delta[\kappa - q_L(u)] = \int_{-3a}^{-a} du h(u) \frac{\delta(u - q_L^{-1}(k))}{|q'_L(u)|} = \frac{h(q_L^{-1}(k))}{q'_L(q_L^{-1}(k))}, \quad (58)$$

where we have removed the modulus in the last step of (58) since $q'_L(u) > 0$ for $u \in [-3a, a)$. Using the expression of $q_L(u)$ in (51), equation (58) further simplifies to

$$H(\kappa) = \frac{\sigma\sqrt{\pi} h(q_L^{-1}(k))}{\exp\left(-\frac{(L+q_L^{-1}(k))^2}{\sigma^2}\right) - \exp\left(-\frac{(L-q_L^{-1}(k))^2}{\sigma^2}\right)} \quad \text{where } \kappa_{\min} \leq \kappa < \kappa^*, \quad (59)$$

with $q_L^{-1}(k)$ being the inverse of the function $q_L(u)$ given in (51), in the range $u \in [-3a, -a)$.

We now analyze $H(\kappa)$ given in (59) near the two edges κ_{\min} and κ^* . We recall that as $\kappa \rightarrow \kappa_{\min}$, i.e., $q_L^{-1}(\kappa) \equiv u \rightarrow -3a$, the limiting behavior of the function $h(u)$ is given in (33), i.e., $h(u)$ diverges as $1/\sqrt{u+3a}$ as $u \rightarrow -3a$. Expanding $q_L(u)$ in Taylor series near $u = -3a$, we get

$$u + 3a = \frac{\kappa - \kappa_{\min}}{q'_L(-3a)} \quad \text{where } q_L(u) = \kappa \quad \text{and} \quad q_L(-3a) = \kappa_{\min}. \quad (60)$$

Therefore using (60) in (33) we get

$$h(q_L^{-1}(k)) \simeq \frac{\tilde{r}}{2\sqrt{a} \sinh(\pi\tilde{r})} \frac{\sqrt{q'_L(-3a)}}{\sqrt{\kappa - \kappa_{\min}}}. \quad (61)$$

Using (61) in (59), as $\kappa \rightarrow \kappa_{\min}$, we get,

$$H(\kappa) \simeq \frac{A_1}{\sqrt{\kappa - \kappa_{\min}}}; \quad A_1 = \frac{\tilde{r}}{2\sqrt{a} \sinh(\pi\tilde{r})} \frac{(\sigma\sqrt{\pi})^{1/2}}{\sqrt{\exp\left(-\frac{(L-3a)^2}{\sigma^2}\right) - \exp\left(-\frac{(L+3a)^2}{\sigma^2}\right)}}. \quad (62)$$

On the other hand, as $\kappa \rightarrow \kappa^*$ from below, $H(\kappa)$ approaches a constant value $H(\kappa^*)$. Using (59) and (32) we get

$$H(\kappa^*) = \frac{\sigma\sqrt{\pi}}{\exp\left(-\frac{(L-a)^2}{\sigma^2}\right) - \exp\left(-\frac{(L+a)^2}{\sigma^2}\right)} \frac{\tilde{r}}{4a \sinh(\pi\tilde{r}/2)} \equiv A_2. \quad (63)$$

3.4.2. Regime II: $\kappa^ \leq \kappa \leq \kappa_{\max}$:* In this regime, where $u \in [-a, a]$, there are two roots of $q_L(u) = \kappa$. Adding the contributions from both roots, we get

$$\begin{aligned} H(\kappa) &= \int_{-a}^a du h(u) \delta[\kappa - q_L(u)] \\ &= \int_{-a}^0 du h(u) \frac{\delta(u - q_L^{-1}(k))}{|q'_L(u)|} + \int_0^a du h(u) \frac{\delta(u - q_L^{-1}(k))}{|q'_L(u)|}, \end{aligned} \quad (64)$$

where $q_L^{-1}(\kappa)$ is the inverse of the function given in (51) in the respective ranges $[-a, 0]$ and $[0, a]$. Since $q_L(u)$ is symmetric about $u = 0$ [see figure 7 and equation (51)], if $u = q_L^{-1}(\kappa)$ denotes the inverse function in $[0, a]$, then the the inverse function in the range $[-a, 0]$ is simply $-u$. Therefore, we get

$$H(\kappa) = \frac{\sigma\sqrt{\pi} [h(q_L^{-1}(k)) + h(-q_L^{-1}(k))]}{\exp\left(-\frac{(L-q_L^{-1}(k))^2}{\sigma^2}\right) - \exp\left(-\frac{(L+q_L^{-1}(k))^2}{\sigma^2}\right)} \quad \text{where } \kappa^* \leq \kappa \leq \kappa_{\max}, \quad (65)$$

with $q_L^{-1}(k) \in [0, a]$ being the inverse of the function $q_L(u)$ given in (51) in the range $u \in [0, a]$.

We now analyze $H(\kappa)$ given in (65) near the two edges κ^* (from above) and κ_{\max} . At $\kappa = \kappa^*$, the two roots of the inverse function $q_L^{-1}(\kappa^*)$ are $-a$ and a . We recall the limiting behavior of the function $h(u)$ near $u = \pm a$ in (33), i.e., $h(u)$ diverges as $1/\sqrt{a-u}$ as $u \rightarrow a$, whereas $h(-a)$ is a constant. Expanding $q_L(u)$ in Taylor series near $u = a$, we get

$$a - u = \frac{\kappa - \kappa^*}{|q'_L(a)|} \quad \text{where } q_L(u) = \kappa \quad \text{and} \quad q_L(a) = \kappa^*. \quad (66)$$

Therefore using (66) in (33), near $q_L^{-1}(k) = a$, we get

$$h(q_L^{-1}(k)) \simeq \frac{\tilde{r}}{2\sqrt{a} \sinh(\pi\tilde{r})} \frac{\sqrt{|q'_L(a)|}}{\sqrt{\kappa - \kappa^*}}. \quad (67)$$

Using (67) in (65), and $q'_L(a) = -q'_L(-a)$, as $\kappa \rightarrow \kappa^*$ from above, we get,

$$H(\kappa) \simeq \frac{A_3}{\sqrt{\kappa - \kappa^*}}; \quad A_3 = \frac{\tilde{r}}{2\sqrt{a} \sinh(\pi\tilde{r})} \frac{(\sigma\sqrt{\pi})^{1/2}}{\sqrt{\exp\left(-\frac{(L-a)^2}{\sigma^2}\right) - \exp\left(-\frac{(L+a)^2}{\sigma^2}\right)}}. \quad (68)$$

Therefore, the scaling function $H(\kappa)$ has a discontinuity at $\kappa = \kappa^*$, namely, $H(\kappa)$ approaches a constant given by (63) as $\kappa \rightarrow \kappa^*$ from below whereas it has a square-root divergence $H(\kappa) \sim 1/\sqrt{\kappa - \kappa^*}$ as $\kappa \rightarrow \kappa^*$ from above as given in (68).

Finally, to analyze $H(\kappa)$ given in (65) near κ_{\max} , we note that near $u = q_L^{-1}(\kappa_{\max}) = 0$, the numerator of (65) approaches a constant whereas the denominator diverges linearly in $u = q_L^{-1}(\kappa)$. Expanding $q_L(u)$ in Taylor series in (51) around $u = 0$, we have $q_L(u) = q_L(0) - (u^2/2)|q''_L(0)| + \dots$. Therefore, as $\kappa \rightarrow \kappa_{\max}$ from above, we have

$$u \equiv q_L^{-1}(\kappa) \simeq \frac{\sqrt{2(\kappa_{\max} - \kappa)}}{\sqrt{|q''_L(0)|}} \quad \text{where } \kappa_{\max} = q_L(0) \quad \text{and} \quad q_L(u) = \kappa, \quad (69)$$

and from (51), $|q''_L(0)| = 4Le^{-L^2/\sigma^2}/(\sqrt{\pi}\sigma^3)$. Therefore, expanding the denominator of (65) in Taylor series, using (69), and $h(0)$ from (32), we get

$$H(\kappa) \simeq \frac{A_4}{\sqrt{\kappa_{\max} - \kappa}}; \quad A_4 = \frac{\sigma^{3/2}\pi^{1/4} e^{L^2/(2\sigma^2)} \tilde{r} \cosh(2\pi\tilde{r}/3)}{\sqrt{2L} \sqrt{3a} \sinh(\pi\tilde{r})}. \quad (70)$$

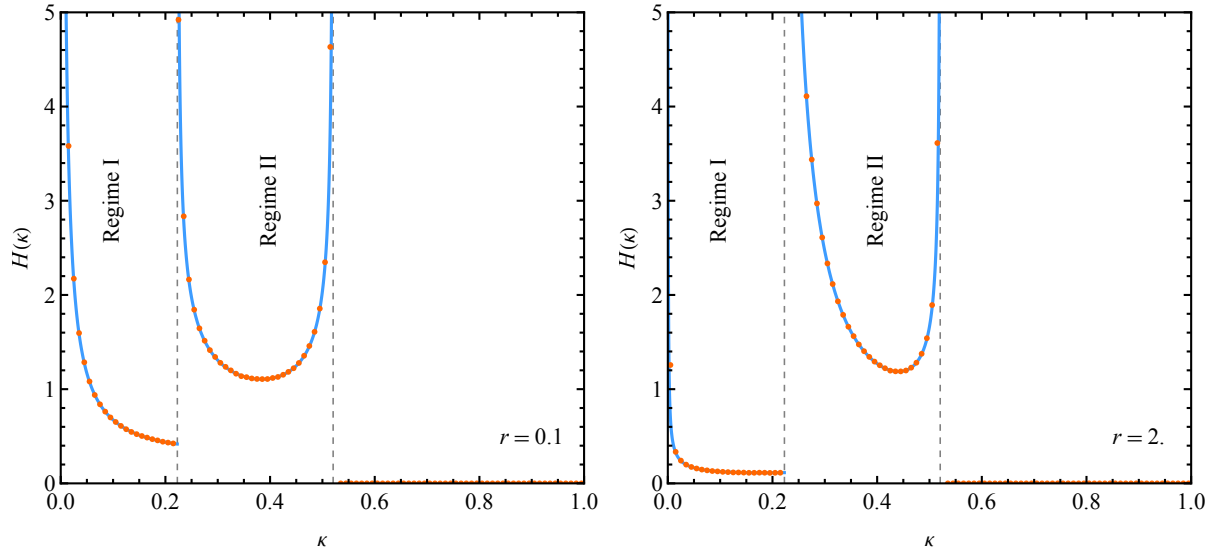


Figure 8. The scaling function $H(\kappa)$ describing the FCS in (54) is plotted against κ for $r = 0.1$ (left) and $r = 2.0$ (right) with $L = 0.5$. The solid lines plot the analytical solutions given in (59) and (65) in the two regimes I and II, respectively. The points are obtained from numerical simulations with 35×10^6 realizations and $N = 10^6$. We set $\omega = 1$, $\sigma = 1$ and $a = 1$. The two dashed vertical lines indicate the positions of $\kappa^* = 0.22\dots$ and $\kappa_{\max} = 0.52\dots$ respectively. The nonzero position of $\kappa_{\min} = 0.0002\dots$ is not visible in the figures. One observes the divergence of $H(\kappa)$ as $\kappa \rightarrow \kappa_{\min}$, $\kappa \rightarrow \kappa^*$ (from the right) and $\kappa \rightarrow \kappa_{\max}$ and the fact that $H(\kappa) \rightarrow \text{const.}$ as $\kappa \rightarrow \kappa^*$ from the left.

We now summarize the FCS discussed in the two regimes (I and II) studied in section 3.4.1 and section 3.4.2. Equation (59) and (65) together give us the FCS. In figure 8, we plot the FCS given in (59) and (65) and also demonstrate excellent agreement with numerics. The scaling function $H(\kappa)$ exhibits a square-root divergence at the two supports κ_{\min} and κ_{\max} as given in (62) and (70) respectively. Moreover, it has a discontinuity at an intermediate point $\kappa_{\min} < \kappa^* < \kappa_{\max}$. As $\kappa \rightarrow \kappa^*$ from below, the scaling function $H(\kappa)$ approaches a constant given in (63). On the other hand, $H(\kappa)$ diverges as $1/\sqrt{\kappa - \kappa^*}$ as $\kappa \rightarrow \kappa^*$ from above, as given in (68). Thus, summarizing,

$$H(\kappa) \simeq \begin{cases} \frac{A_1}{\sqrt{\kappa - \kappa_{\min}}} & \text{as } \kappa \rightarrow \kappa_{\min} \\ A_2 & \text{as } \kappa \rightarrow \kappa^* \text{ from below/left} \\ \frac{A_3}{\sqrt{\kappa - \kappa^*}} & \text{as } \kappa \rightarrow \kappa^* \text{ from above/right} \\ \frac{A_4}{\sqrt{\kappa_{\max} - \kappa}} & \text{as } \kappa \rightarrow \kappa_{\max} \end{cases} \quad (71)$$

where the constants A_1 , A_2 , A_3 , and A_4 are given in (62), (63), (68) and (70) respectively.

3.4.3. Generalizing FCS to arbitrary domain $[L_1, L_2]$: Now, we generalize the FCS to arbitrary domain $[L_1, L_2]$. It is worth noting that the special case $L_1 = 0, L_2 \rightarrow \infty$ is referred to as the “index problem”. For the arbitrary domain case, as in the FCS in (54), the probability of finding N_{L_1, L_2} number of particles in a domain $[L_1, L_2]$ is given by

$$P(N_{L_1, L_2}, N) \simeq \frac{1}{N} H\left(\frac{N_{L_1, L_2}}{N}\right) \quad \text{with} \quad H(\kappa) = \int_{-3a}^a du h(u) \delta[\kappa - q(u, L_1, L_2)], \quad (72)$$

where $q(u, L_1, L_2)$ is given by [generalization of the special case in (51)]

$$q(u, L_1, L_2) = \int_{L_1}^{L_2} \frac{1}{\sqrt{\pi\sigma^2}} e^{-\frac{1}{2\sigma^2}(x_j - u)^2} dx = \frac{1}{2} \left[\operatorname{erf}\left(\frac{u - L_1}{\sigma}\right) + \operatorname{erf}\left(\frac{L_2 - u}{\sigma}\right) \right]. \quad (73)$$

As before, in order to carry out the integral in (72), we need to invert the function $q(u, L_1, L_2)$ in (73). It is useful to elucidate $q(u, L_1, L_2)$ as a function of u for different domains of $[L_1, L_2]$. As evident from figure 9, depending on the domain, the function $q(u, L_1, L_2)$ is either single-valued or multi-valued in the range $u \in [-3a, a]$. Subsequently, the function can be inverted as described above for the symmetric domain $[-L, L]$.

Finally, we note that for in the “index problem”, setting $L_1 = 0$ and $L_2 \rightarrow \infty$ in (73), we get $q(u, 0, \infty) = [1 + \operatorname{erf}(u/\sigma)]/2$ which turns out to be a single valued function. Therefore, from (72), the scaling function for the distribution of the index fraction $N_{0, \infty}/N$ is given by,

$$H(\kappa) = \sqrt{\pi} \sigma e^{u(\kappa)^2/\sigma^2} h(u(\kappa)), \quad \text{where} \quad u(\kappa) = \sigma \operatorname{erf}^{-1}(2\kappa - 1), \quad (74)$$

with erf^{-1} being the inverse error function, i.e., $\operatorname{erf}[\operatorname{erf}^{-1}(z)] = \operatorname{erf}^{-1}[\operatorname{erf}(z)] = z$ and $\operatorname{erf}^{-1}(z) = -\operatorname{erf}^{-1}(-z)$. The scaling function $H(\kappa)$ in (74) for the index distribution is supported in the finite range $\kappa \in [(1 - \operatorname{erf}(3a/\sigma))/2, (1 + \operatorname{erf}(a/\sigma))/2]$.

4. Numerical simulation procedure

In our numerical simulations, we draw the random variables directly from the stationary JPDF (25). To generate the set of correlated random variables with a common random mean u , we follow the steps below for each realization of the simulation.

- (i) We first draw a random time τ from the exponential distribution $r e^{-r\tau}$.
- (ii) We then construct another random variable u from τ using (24).
- (iii) Next, we draw N Gaussian random variables $\{x_1, x_2, \dots, x_N\}$ independently with a common mean u and variance σ^2 .

We repeat steps (i)–(iii) to generate an ensemble of random variables according to the JPDF given in (25). We use this ensemble of random variables to obtain the statistics of the observables of our interest discussed in sections 3.1–3.4. Figure 2 verifies that the PDF of the random mean u generated by using a large number of realizations of steps (i) and (ii) indeed agrees with $h(u)$ given in (32).

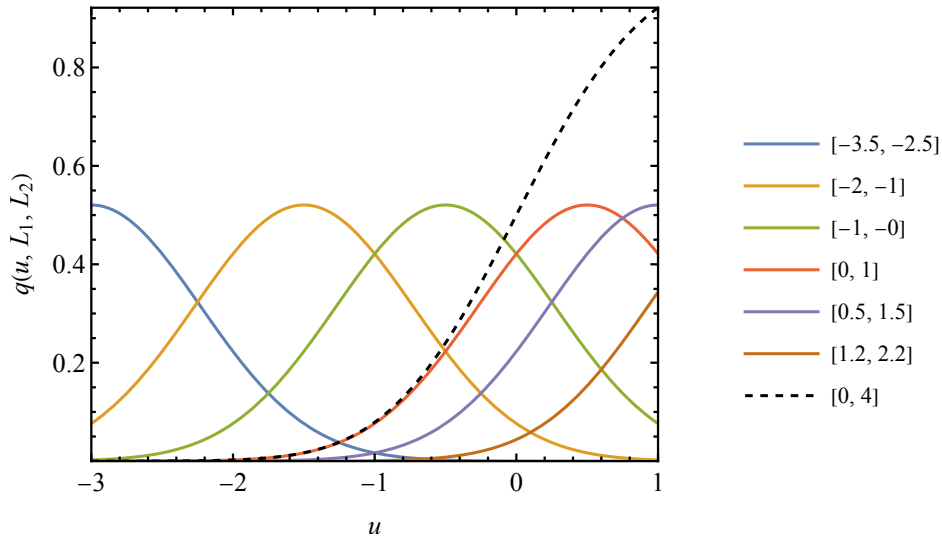


Figure 9. Plots of $\kappa = q(u, L_1, L_2)$ given in (73) as a function of u , for various domains $[L_1, L_2]$ mentioned in the legend. The black dashed line is the special case close to the “index problem”, i.e., $L_1 = 0$ and $L_2 \rightarrow \infty$.

5. Summary and Outlook

To summarize, we investigated a system of N noninteracting bosons in one dimension that are simultaneously subjected to resetting with a rate r . The initial state is the ground state of a harmonic oscillator centered around a position ($x = a$) and the time evolution is with a different Hamiltonian, more precisely, an oscillator centered around another location ($x = -a$). The subsequent unitary dynamics is interrupted by simultaneously resetting all the bosons back to the initial state, which results in emergent strong attractive correlations. We showed that the system reaches a nonequilibrium stationary state with a joint distribution that is non-factorizable. We demonstrated that the stationary joint distribution has a conditionally independent and identically distributed (CIID) structure, given in (15), which we further exploited to compute several observables analytically. The density profile in figure 3 shows an interesting bimodal to unimodal transition. In figure 4 we show the quantum dynamics of the density profile and its eventual approach to steady state in the presence of resetting. To unravel the effects of these correlations, we computed the two-point correlation functions [equation (40)], order statistics [figure 5], and the full counting statistics [figure 8]. The results of these quantities are very distinct from that of uncorrelated or weakly correlated bosons indicating the dynamical emergence of a strongly correlated Bose gas. In particular, the FCS exhibits rather surprising features. First, in the thermodynamic limit, the lower support κ_{\min} of the scaling function describing the FCS is strictly greater than zero, and the upper support κ_{\max} is strictly less than unity. This indicates that a given region $[-L, L]$ can neither be completely empty nor completely full. The second surprising feature is that there is a discontinuity of the scaling function at an intermediate fraction $\kappa_{\min} < \kappa^* < \kappa_{\max}$. The scaling function diverges as $\kappa \rightarrow \kappa^*$ from

above, whereas it approaches a constant when κ approaches κ^* from below.

The focus of this work was on noninteracting bosons in a harmonic trap subjected to quantum resetting. There are many new interesting future directions one can pursue. For example, it will be interesting to extend our study to trapped noninteracting fermions subjected to a similar quantum resetting protocol where the Pauli exclusion principle will play an important role. It will also be interesting to consider a protocol where the center of the harmonic trap is repeatedly switched back and forth [17] instead of the strict instantaneous reset protocol considered in this work. Realizing our results in experiments will be interesting. In this work, we restricted ourselves to noninteracting bosons. It would be further interesting to explore quantum resetting in interacting systems where the correlations between two particles in the nonequilibrium stationary state has two origins: (i) due to the inherent interactions between the particles and (ii) generated dynamically by the simultaneous quantum resetting. It will be interesting to study the combined effects of (i) and (ii).

6. Acknowledgements

We thank G. Schehr for useful discussions. M. K. acknowledges the support of the Department of Atomic Energy, Government of India, under project no. RTI4001. M. K. thanks the VAJRA faculty scheme (No. VJR/2019/000079) from the Science and Engineering Research Board (SERB), Department of Science and Technology, Government of India. S. N. M. and S. S. acknowledges the support from the Science and Engineering Research Board (SERB, Government of India), under the VAJRA faculty scheme (No. VJR/2017/000110). M. K. and S. S. thank the hospitality of Laboratoire de Physique Théorique et Modèles Statistiques (LPTMS), University Paris-Saclay where a major part of the work took place. We thank the support from the International Research Project (IRP) titled ‘Classical and quantum dynamics in out of equilibrium systems’ by CNRS, France. M. K. thanks the hospitality of Raman Research Institute, Bangalore. M. K. and S. S. thank the hospitality of Laboratoire de Physique Théorique et Hautes Energies (LPTHE), Sorbonne Université, Paris, France.

References

- [1] Dalfovo, F., Giorgini, S., Pitaevskii, L.P. and Stringari, S. 1999 Theory of Bose-Einstein condensation in trapped gases *Rev. Mod. Phys.* **71** 463.
- [2] Blakie, P.B., Bradley, A.S., Davis, M.J., Ballagh, R.J. and Gardiner, C.W. 2008 Dynamics and statistical mechanics of ultra-cold Bose gases using c-field techniques *Adv. Phys.* **57** 363.
- [3] Levin, K., Levin, K., Fetter, A. and Stamper-Kurn, D. eds. 2012 Ultracold Bosonic and Fermionic Gases (Vol. 5). Elsevier.
- [4] Lieb, E.H. and Liniger, W. 1963 *Phys. Rev.* **130** 1605.
- [5] Lieb, E.H. 1963 Exact analysis of an interacting Bose gas. II. The excitation spectrum *Phys. Rev.* **130** 1616.

- [6] Sutherland, B. 2004 Beautiful models: 70 years of exactly solved quantum many-body problems. World Scientific.
- [7] Pethick, C.J. and Smith, H. 2008 Bose–Einstein condensation in dilute gases. Cambridge University Press.
- [8] Pitaevskii, L. and Stringari, S. 2003 Bose-Einstein Condensation. Oxford University Press.
- [9] Erdős, L., Schlein, B. and Yau, H.T. 2007 Rigorous derivation of the Gross-Pitaevskii equation *Phys. Rev. Lett.* **98** 040404.
- [10] Calabrese, P. and Caux, J.S. 2007 Dynamics of the attractive 1D Bose gas: analytical treatment from integrability *J. Stat. Mech.* P08032.
- [11] Calabrese, P. and Caux, J.S. 2007 Correlation functions of the one-dimensional attractive Bose gas *Phys. Rev. Lett.* **98** 150403.
- [12] Panfil, M. and Caux, J.S. 2014 Finite-temperature correlations in the Lieb-Liniger one-dimensional Bose gas *Phys. Rev. A* **89** 033605.
- [13] De Nardis, J. and Panfil, M. 2016 Exact correlations in the Lieb-Liniger model and detailed balance out-of-equilibrium *SciPost Phys.* **1** 015.
- [14] Biroli, M., Larralde, H., Majumdar, S.N. and Schehr, G. 2023 Extreme statistics and spacing distribution in a Brownian gas correlated by resetting *Phys. Rev. Lett.* **130** 207101.
- [15] Biroli, M., Larralde, H., Majumdar, S.N. and Schehr, G. 2024 Exact extreme, order, and sum statistics in a class of strongly correlated systems *Phys. Rev. E* **109** 014101.
- [16] Biroli, M., Kulkarni, M., Majumdar, S.N. and Schehr, G. 2024 Dynamically emergent correlations between particles in a switching harmonic trap *Phys. Rev. E* **109** L032106.
- [17] Sabhapandit, S. and Majumdar, S.N. 2024 Noninteracting particles in a harmonic trap with a stochastically driven center *arXiv preprint arXiv:2404.02480*.
- [18] Evans, M.R. and Majumdar, S.N. 2011 Diffusion with stochastic resetting *Phys. Rev. Lett.* **106** 160601.
- [19] Evans, M.R. and Majumdar, S.N. 2011 Diffusion with optimal resetting *J. Phys. A: Math. Theor.* **44** 435001.
- [20] Evans, M.R., Majumdar, S.N. and Schehr, G. 2020 Stochastic resetting and applications *J. Phys. A: Math. Theor.* **53** 193001.
- [21] Gupta, S. and Jayannavar, A.M. 2022 Stochastic resetting: A (very) brief review. *Front. Phys.* **10** 789097.
- [22] Kundu, A. and Reuveni, S. 2024 Preface: stochastic resetting—theory and applications *J. Phys. A: Math. Theor.* **57** 060301.
- [23] Mukherjee, B., Sengupta, K. and Majumdar, S.N. 2018 Quantum dynamics with stochastic reset *Phys. Rev. B* **98** 104309.
- [24] Rose, D. C., Touchette, H., Lesanovsky, I., and Garrahan, J. P. 2018 Spectral properties of simple classical and quantum reset processes *Phys. Rev. E* **98** 022129.
- [25] Perfetto, G., Carollo, F., Magoni, M. and Lesanovsky, I. 2021 Designing nonequilibrium states of quantum matter through stochastic resetting *Phys. Rev. B* **104** L180302.
- [26] Dattagupta, S., Das, D. and Gupta, S., 2022. Stochastic resets in the context of a tight-binding chain driven by an oscillating field. *J. Stat. Mech.* 103210.
- [27] Perfetto, G., Carollo, F., Lesanovsky, I. 2022 Thermodynamics of quantum-jump trajectories of open quantum systems subject to stochastic resetting *SciPost Phys.* **13** 079.
- [28] Magoni, M., Carollo, F., Perfetto, G. and Lesanovsky, I. 2022 Emergent quantum correlations and collective behavior in noninteracting quantum systems subject to stochastic resetting *Phys. Rev. A* **106** 052210.
- [29] Turkeshi, X., Dalmonte, M., Fazio, R. and Schiro, M. 2022 Entanglement transitions from stochastic resetting of non-Hermitian quasiparticles *Phys. Rev. B* **105** L241114.
- [30] Dubey, V., Chetrite, R., and Dhar, A. 2023 Quantum resetting in continuous measurement induced dynamics of a qubit *J. Phys. A: Math. Theor.* **56** 154001.
- [31] Sevilla, F.J. and Valdés-Hernández, A. 2023 Dynamics of closed quantum systems under stochastic

- resetting *J. Phys. A: Math. Theor.* **56** 034001.
- [32] Yin, R. and Barkai, E. 2023 Restart expedites quantum walk hitting times *Phys. Rev. Lett* **130** 050802.
 - [33] Kulkarni, M. and Majumdar, S.N. 2023 Generating entanglement by quantum resetting. *Phys. Rev. A* **108** 062210.
 - [34] Kulkarni, M. and Majumdar, S.N. 2023 First detection probability in quantum resetting via random projective measurements. *J. Phys. A: Math. Theor.* **56** 385003.
 - [35] Yin, R., Wang, Q. and Barkai, E. 2024 Instability in the quantum restart problem. *Phys. Rev. E* **109** 064150.
 - [36] Cornish, S.L., Claussen, N.R., Roberts, J.L., Cornell, E.A. and Wieman, C.E. 2000 Stable ^{85}Rb Bose-Einstein condensates with widely tunable interactions *Phys. Rev. Lett.* **85** 1795.
 - [37] Roati, G., Zaccanti, M., d'Errico, C., Catani, J., Modugno, M., Simoni, A., Inguscio, M. and Modugno, G. 2007 ^{39}K Bose-Einstein condensate with tunable interactions *Phys. Rev. Lett.* **99** 010403.
 - [38] Besga, B., Bovon, A., Petrosyan, A., Majumdar, S.N. and Ciliberto, S. 2020 Optimal mean first-passage time for a Brownian searcher subjected to resetting: experimental and theoretical results *Phys. Rev. Res.* **2** 032029.
 - [39] Faisant, F., Besga, B., Petrosyan, A., Ciliberto, S. and Majumdar, S.N. 2021 Optimal mean first-passage time of a Brownian searcher with resetting in one and two dimensions: experiments, theory and numerical tests *J. Stat. Mech.* 113203.
 - [40] Forrester P J 2010 Log-gases and random matrices (LMS-34), Princeton University Press.
 - [41] Mehta M L 2004 Random matrices, Elsevier.
 - [42] Marino, R., Majumdar, S.N., Schehr, G. and Vivo, P. 2014 Phase transitions and edge scaling of number variance in Gaussian random matrices *Phys. Rev. Lett.* **112** 254101.
 - [43] Leblé, T. and Serfaty, S. 2017 Large deviation principle for empirical fields of Log and Riesz gases *Invent. Math.* **210** 645.
 - [44] Majumdar, S.N. and Schehr, G. 2014 Top eigenvalue of a random matrix: large deviations and third order phase transition *J. Stat. Mech.* 01012.
 - [45] Majumdar, S.N., Nadal, C., Scardicchio, A. and Vivo, P. 2009 Index distribution of Gaussian random matrices *Phys. Rev. Lett.* **103** 220603.
 - [46] Agarwal, S., Kulkarni, M. and Dhar, A. 2019 Some connections between the classical Calogero–Moser model and the log-gas *J. Stat. Phys.* **176** 1463.
 - [47] Dhar, A., Kundu, A., Majumdar, S.N., Sabhapandit, S. and Schehr, G. 2017 Exact extremal statistics in the classical 1d Coulomb gas *Phys. Rev. Lett.* **119** 060601.
 - [48] Dhar, A., Kundu, A., Majumdar, S.N., Sabhapandit, S. and Schehr, G. 2018 Extreme statistics and index distribution in the classical 1d Coulomb gas *J. Phys. A: Math. Theor.* **51** 295001.
 - [49] Flack, A., Majumdar, S.N. and Schehr, G. 2021 Truncated linear statistics in the one dimensional one-component plasma *J. Phys. A: Math. Theor.* **54** 435002.
 - [50] Flack, A., Majumdar, S.N. and Schehr, G. 2022 Gap probability and full counting statistics in the one-dimensional one-component plasma *J. Stat. Mech.* 053211.
 - [51] Hardin, D.P., Leblé, T., Saff, E.B. and Serfaty, S. 2018 Large deviation principles for hypersingular Riesz gases *Constr. Approx.* **48** 61.
 - [52] Agarwal, S., Dhar, A., Kulkarni, M., Kundu, A., Majumdar, S.N., Mukamel, D. and Schehr, G. 2019 Harmonically confined particles with long-range repulsive interactions *Phys. Rev. Lett.* **123** 100603.
 - [53] Kumar, A., Kulkarni, M. and Kundu, A. 2020 Particles confined in arbitrary potentials with a class of finite-range repulsive interactions *Phys. Rev. E* **102** 032128.
 - [54] Kethepalli, J., Kulkarni, M., Kundu, A., Majumdar, S.N., Mukamel, D. and Schehr, G. 2022 Edge fluctuations and third-order phase transition in harmonically confined long-range systems *J. Stat. Mech.* 033203.
 - [55] Santra, S., Kethepalli, J., Agarwal, S., Dhar, A., Kulkarni, M. and Kundu, A. 2022 Gap statistics

- for confined particles with power-law interactions *Phys. Rev. Lett.* **128** 170603.
- [56] Kethepalli, J., Kulkarni, M., Kundu, A., Majumdar, S.N., Mukamel, D. and Schehr, G. 2024 Full counting statistics of 1d short-range Riesz gases in confinement *arXiv preprint* arXiv:2403.18750.
 - [57] Ketterle, W. 1999 Experimental studies of Bose-Einstein condensation *Phys. Today* **52** 30.
 - [58] Smith, D.A., Aigner, S., Hofferberth, S., Gring, M., Andersson, M., Wildermuth, S., Krüger, P., Schneider, S., Schumm, T. and Schmiedmayer, J. 2011 Absorption imaging of ultracold atoms on atom chips *Opt. Exp.* **19** 8471.
 - [59] Hueck, K., Luick, N., Sobirey, L., Siegl, J., Lompe, T., Moritz, H., Clark, L.W. and Chin, C. 2017 Calibrating high intensity absorption imaging of ultracold atoms *Opt. Exp.* **25** 8670.
 - [60] Kulkarni, M. and Abanov, A.G. 2012 Hydrodynamics of cold atomic gases in the limit of weak nonlinearity, dispersion, and dissipation *Phys. Rev. A* **86** 033614.
 - [61] Gross, C. and Bakr, W.S. 2021 Quantum gas microscopy for single atom and spin detection *Nat. Phys.* **17** 1316.
 - [62] Bakr, W.S., Peng, A., Tai, M.E., Ma, R., Simon, J., Gillen, J.I., Foelling, S., Pollet, L. and Greiner, M. 2010 Probing the superfluid-to-mott insulator transition at the single-atom level. *Science* **329** 547.
 - [63] Sherson, J.F., Weitenberg, C., Endres, M., Cheneau, M., Bloch, I. and Kuhr, S. 2010 Single-atom-resolved fluorescence imaging of an atomic Mott insulator *Nature* **467** 68.
 - [64] Buob, S., Höschele, J., Makhlov, V., Rubio-Abadal, A. and Tarruell, L. 2024 A strontium quantum-gas microscope *Phys. Rev. X Quan.* **5** 020316.
 - [65] Feynman, R.P., Hibbs, A.R. and Styer, D.F. 2010 Quantum mechanics and path integrals. Courier Corporation.
 - [66] Majumdar, S.N., Pal, A. and Schehr, G. 2020 Extreme value statistics of correlated random variables: a pedagogical review *Phys. Rep.* **840** 1.
 - [67] Majumdar, S.N., Schehr, G. 2024 Statistics of Extremes and Records in Random Sequences. Oxford University Press.
 - [68] Sabhapandit, S., Majumdar, S.N. and Redner, S. 2008 Crowding at the front of marathon packs *J. Stat. Mech.* 03001.
 - [69] Sabhapandit, S. 2019 Extremes and records. *arXiv preprint* arXiv:1907.00944.